A NONSMOOTH GRAPH-BASED APPROACH TO LIGHT FIELD SUPER-RESOLUTION

Mattia Rossi *Mireille El Gheche* *Pascal Frossard*

École Polytechnique Fédérale de Lausanne (EPFL)
Signal Processing Laboratory (LTS4)

ABSTRACT

We propose a new super-resolution algorithm tailored for light field cameras, which suffer by design from a limited spatial resolution. In particular, we cast light field super-resolution into an optimization problem, where the particular structure of the light field data is captured by a nonsmooth graph-based regularizer, and where all the light field views are super-resolved jointly. Our experiments show that the proposed method compares favorably to the state-of-the-art light field super-resolution algorithms in terms of PSNR and visual quality. In particular, the nonsmooth graph-based regularizer leads to sharper images while preserving fine details.

Index Terms— light field, super-resolution, graph

1. INTRODUCTION

A light field camera behaves as a compact camera array, providing multiple simultaneous images of a 3D scene from slightly different points of view on a regular grid [1]. The captured data is referred to as the *light field* [2] and is potentially suitable for a wide range of applications, such as depth estimation, view synthesis, and 3D modeling. However, the light field views exhibit a significantly lower resolution than images from traditional cameras, and this represents a limit for many light field applications. It is therefore crucial to improve the resolution of the light field views through super-resolution techniques.

It is important to note that the light field data is characterized by a particular structure that needs to be preserved when augmenting the resolution of the single light field views. As a consequence, off-the-shelf single-frame super-resolution algorithms [3–5], which are completely blind to the light field structure, and traditional multi-frame super-resolution algorithms [6–8], whose global warping model is too general to capture the complexity of the light field structure, are not ideal candidates for light field super-resolution. Motivated by this observation, in this article we present a new super-resolution algorithm which explicitly takes the light field structure into account by modeling the inter-view correlation with a graph.

A few super-resolution algorithms developed explicitly for light field data have already been proposed in the literature, but they exhibit one or more drawbacks. For example, in their light field super-resolution framework [9], Wanner and Goldluecke propose to compute a disparity map with subpixel precision at each low resolution view of the light field, and then, to use the computed maps to sequentially super-resolve each light field view within a multi-frame alike super-resolution method. However, disparity estimation is a very challenging task at low spatial resolution and the disparity errors translate into significant artifacts in the super-resolved light field views.

In a different framework, Mitra and Veeraraghavan propose a light field super-resolution algorithm based on a learning procedure [10]. The low resolution light field is decomposed into multiple light fields with small spatial resolution, referred to as *light field patches*, and each one is assigned a unique disparity value. A *Gaussian Mixture Model* prior for light field patches is learnt offline for each disparity value and then employed, within a *MAP* estimator, to super-resolve each light field patch. However, first, the reconstruction quality depends on the selected light field training data, which is not readily available yet; second, the constant disparity assumption within each patch leads to severe artifacts at depth discontinuities in the super-resolved light field views.

Building on our previous work [11,12], we propose a new light field super-resolution algorithm that targets the drawbacks of the methods in [9,10]. We develop a super-resolution algorithm that augments the resolution of all the views together, while relying only on a very rough estimate of the disparity at each view, and without any offline learning procedure. In particular, *light field super-resolution* is casted into a global optimization problem, whose objective function comprises three terms. The first one enforces data fidelity, by constraining each high resolution view to be consistent with its low resolution counterpart. The second one is a warping term, which gathers for each view the complementary information encoded in the others. The third one is a novel graph-based prior, which regularizes the high resolution views by enforcing the geometric structure of the light field. Differently from our previous work [12], where a quadratic graph-based regularizer is employed, the new graph-based regularizer is nonsmooth. This represents a substantial difference, as quadratic regularizers are known to induce a low-pass filtered solution, while the adopted nonsmooth regularizer does not; it better preserves textures, edges, and fine structures in

general. We solve the new optimization problem using the *Forward-Backward Primal-Dual* method [13], and we show that the new algorithm leads to significantly better reconstruction results, especially in terms of visual quality.

2. THE LIGHT FIELD

We first introduce the framework studied in this paper. We consider the light field $\boldsymbol{U}$ as the output of an $M \times M$ array of cameras, each one equipped with an $N \times N$ pixel sensor. We denote with $\boldsymbol{U}_k \in \mathbb{R}^{N \times N}$ the k-th view in the light field in column major order, with $k \in \{1, 2, ..., M^2\}$. Also, we denote with $\boldsymbol{U}_k(x, y) \in \mathbb{R}$ the intensity of the pixel at (x, y) within the same view, with $x, y \in \{1, 2, ..., N\}$.

The particular light field structure is summarized in Figure 1. Under the *Lambertian* assumption, the projections of a pixel $\boldsymbol{U}_k(x, y)$ on the eight surrounding views fall on a virtual square (in red in Figure 1) whose size depends on the disparity value $d_{x,y}$ associated to $\boldsymbol{U}_k(x, y)$, with $d_{x,y}$ not necessarily integer. This is referred to as the *Square Constraint* in [12]. In particular, due to the registration of the light field views, the projection of the pixel $\boldsymbol{U}_k(x, y)$ falls along a row or a column in the horizontally and vertically adjacent views, respectively, while it falls along a diagonal trajectory in the four diagonally adjacent views. Later on, we will refer to this configuration as the *light field structure*.

3. PROBLEM FORMULATION

The light field super-resolution problem deals with the recovery of the high resolution views $\boldsymbol{U}_k \in \mathbb{R}^{N \times N}$ of the light field $\boldsymbol{U}$ from the corresponding low resolution views $\boldsymbol{V}_k \in \mathbb{R}^{(N/\alpha) \times (N/\alpha)}$ of the light field $\boldsymbol{V}$, with $\alpha \in \mathbb{Z}^+$ the *super-resolution factor*. We cast the super-resolution problem into the minimization of the following objective function:

$$\boldsymbol{u}^* \in \underset{\boldsymbol{u}}{\operatorname{argmin}} \; f_1(\boldsymbol{u}) + \lambda_2 f_2(\boldsymbol{u}) + \lambda_g g(\boldsymbol{u}) \quad (1)$$

where λ_2 and λ_g are positive constants balancing the three terms. Hereafter, $\boldsymbol{u}_k$ and $\boldsymbol{u}$ denote the vectorized versions of the view $\boldsymbol{U}_k$ and of the whole light field $\boldsymbol{U}$, respectively.

The first term in Eq. (1) enforces the consistency between the high and low resolution versions of the same view, and it is typically referred to as the *data fidelity term*:

$$f_1(\boldsymbol{u}) = \sum_k \|\boldsymbol{SB}\,\boldsymbol{u}_k - \boldsymbol{v}_k\|_2^2. \quad (2)$$

where $\boldsymbol{B} \in \mathbb{R}^{N^2 \times N^2}$ and $\boldsymbol{S} \in \mathbb{R}^{(N/\alpha)^2 \times N^2}$ denote a blurring and a sampling matrix, respectively.

The various low resolution views in the light field capture the scene from slightly different perspectives, therefore, details dropped by digital sensor sampling at one view may survive in another one. In order to gather at one view the complementary information from the others, we can enforce that each high resolution view $\boldsymbol{u}_k$ can generate, by warping, the other low resolution views $\boldsymbol{v}_{k'}$ in the light field, with $k' \neq k$. This is the purpose of the second term in Eq. (1):

$$f_2(\boldsymbol{u}) = \sum_k \sum_{k' \in \mathcal{N}_k^+} \|\boldsymbol{SB}\boldsymbol{F}_k^{k'}\,\boldsymbol{u}_k - \boldsymbol{v}_{k'}\|_2^2 \quad (3)$$

where the matrix $\boldsymbol{F}_k^{k'} \in \mathbb{R}^{N^2 \times N^2}$ is such that $\boldsymbol{F}_k^{k'}\boldsymbol{u}_k \simeq \boldsymbol{u}_{k'}$ and it is typically referred to as a *warping matrix*, while $\mathcal{N}_k^+$ denotes the set of the four views horizontally and vertically adjacent to $\boldsymbol{u}_k$, which are colored in orange in Figure 1. We do not rely on a precise estimate of the warping matrices, as this would require us to carry out an expensive disparity estimation with sub-pixel precision at each light field view. We rather adopt the coarse *Square Constraint* estimation method in [12], which relies only on a rough disparity estimation step, as the noise introduced by the imprecise warping matrices is handled by the third term in Eq. (1), our regularizer.

As anticipated, the third term in Eq. (1) is a regularizer. It models each pixel in the high resolution light field as a vertex of a graph, where edges connect one pixel to its projections on the other eight surrounding views, as shown in Figure 1.

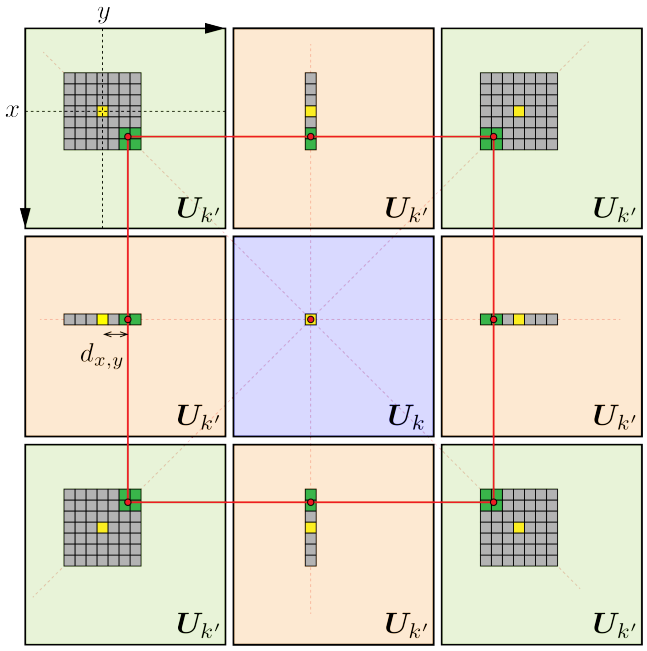

Fig. 1. The light field structure. The tiny squares indicate pixels, and those in yellow lie at (x, y). Each rectangular cluster of pixels is a search window: 1D at the orange views, 2D at the green ones. The projection of the pixel $U_k(x, y)$ on the eight surrounding views is denoted with a red dot. The projections lie on a red virtual square determined by the disparity $d_{x,y}$ associated to $U_k(x, y)$. The projections fall between two adjacent pixels in the orange views, and within four adjacent pixels in the green views. These pixels are highlighted in green and are those connected to $U_k(x, y)$ in the graph.

Formally, we define the regularizer as follows [14]:

$$g(\boldsymbol{u}) \;=\; \sum_i \sqrt{\sum_{j\sim i} w(i,j)\,(\boldsymbol{u}(i)-\boldsymbol{u}(j))^2} \qquad (4)$$

where $w(i,j)>0$ is an edge weight capturing the similarity between the pixels $\boldsymbol{u}(i)$ and $\boldsymbol{u}(j)$, with $j\sim i$ the set of pixels $\boldsymbol{u}(j)$ directly connected to $\boldsymbol{u}(i)$. The regularizer in Eq. (4) enforces the directly connected pixels in the graph, i.e. those which are the projection of the same 3D point in the scene, to share similar intensity values, thus promoting the light field structure. The square root in the nonsmooth regularizer of Eq. (4) is chosen in order not to over penalize those pixels whose intensity differ significantly from that of its directly connected neighbors in the graph. This prevents the low-pass tendency of the quadratic regularizer in our work [12].

In practice, as shown in Figure 1, the projection of a pixel $\boldsymbol{U}_k(x,y)$ in a neighboring view $\boldsymbol{U}_{k'}$ does not lie at integer spatial coordinates. Therefore, in our graph, we aim at connecting the pixel $\boldsymbol{U}_k(x,y)$ to the n pixels of $\boldsymbol{U}_{k'}$ that enclose its projection. These pixels are indicated in green in Figure 1: n is 2 for the horizontally and vertically adjacent views and 4 for the diagonally adjacent ones. To detect these pixels, we center a search window at the pixel $\boldsymbol{U}_{k'}(x,y)$, and we compute the following weight between the pixel $\boldsymbol{U}_k(x,y)=\boldsymbol{u}(i)$ and each pixel $\boldsymbol{U}_{k'}(x',y')=\boldsymbol{u}(j)$ in the window:

$$w(i,j) \;=\; \exp\left(-\frac{\|\mathcal{P}_k(x,y)-\mathcal{P}_{k'}(x',y')\|_F^2}{\sigma^2}\right), \qquad (5)$$

where $\mathcal{P}_k(x,y)$ is a square patch centered at $\boldsymbol{U}_k(x,y)$, $\|\cdot\|_F$ is the Frobenius norm, and σ is a tunable constant. The procedure is repeated for each one of the eight surrounding views. The shape of the search window varies from view to view: a 1D search window is sufficient for the horizontally and vertically adjacent views, while a 2D window is preferred for the diagonally adjacent ones, as shown in Figure 1. Finally, among the weights computed for the adjacent view $\boldsymbol{U}_{k'}$, we keep only the n highest ones, with n equal to 2 and 4 for the views $\boldsymbol{U}_{k'}$ equipped with a 1D and a 2D window, respectively.

4. SUPER-RESOLUTION ALGORITHM

We now have all the ingredients to solve our problem in Eq. (1), whose objective function is the sum of a smooth function $f=f_1+\lambda_2\,f_2$ and a nonsmooth one $\lambda_g\,g$. In particular, the nonsmooth function g can be expressed as the $\ell_{1,2}$-norm composed with a discrete difference operator:

$$g(\boldsymbol{u}) \;=\; \|\boldsymbol{T}\boldsymbol{u}\|_{1,2} \qquad (6)$$

where

$$\boldsymbol{T}\boldsymbol{u} \;=\; \begin{bmatrix} \Big[\sqrt{w(1,j)}(\boldsymbol{u}(1)-\boldsymbol{u}(j))\Big]_{j\sim 1} \\ \vdots \\ \Big[\sqrt{w((NM)^2,j)}(\boldsymbol{u}((NM)^2)-\boldsymbol{u}(j))\Big]_{j\sim (NM)^2} \end{bmatrix}$$

and the i-th row in the above formula is a vector in $\mathbb{R}^{|j\sim i|}$, with $|\cdot|$ the set cardinality. As a consequence, the solution of the problem in Eq. (1) requires an algorithm to deal with convex problems involving nonsmooth functions and linear operators. For this reason, we resort here to *Primal-Dual Proximal Methods* [13, 15–19]. In the convex setting, the key tool of these methods is the proximity operator [20] of a lower semi-continuous convex function $\varphi\colon \mathbb{R}^K \mapsto]-\infty;+\infty]$, defined as $\text{prox}_{\varphi}(\bar{\boldsymbol{z}}) = \text{argmin}_{\boldsymbol{z}}\ \varphi(\boldsymbol{z}) + (1/2)\|\boldsymbol{z}-\bar{\boldsymbol{z}}\|^2, \forall \bar{\boldsymbol{z}}\in\mathbb{R}^K$. Proximal methods provide a unifying framework that permits to address a wide class of convex optimization problems involving nonsmooth penalizations and hard constraints.

We solve the problem in Eq. (1) using the *Forward-Backward Primal-Dual (FBPD)* method [13], due to its straightforward implementation. In the FBPD method, detailed in Algorithm 1, each iteration evaluates the gradient ∇f of the function $f=f_1+\lambda_2\,f_2$ and the proximity operator of the $\ell_{1,2}$-norm. The gradient ∇f is defined as follows:

$$\nabla f(\boldsymbol{u}) \;=\; 2\sum_k (\boldsymbol{S}\boldsymbol{B})^\top(\boldsymbol{S}\boldsymbol{B}\boldsymbol{u}_k-\boldsymbol{v}_k) \;+\; 2\sum_k\sum_{k'\in\mathcal{N}_k^+}\lambda_2\left(\boldsymbol{S}\boldsymbol{B}\boldsymbol{F}_{k'}^k\right)^\top\left(\boldsymbol{S}\boldsymbol{B}\boldsymbol{F}_{k'}^k\boldsymbol{u}_{k'}-\boldsymbol{v}_k\right).$$

The $\ell_{1,2}$-norm proximity operator is listed in [21, Eq. (16)].

Algorithm 1 FBPD [13]

Initialization

Choose $\boldsymbol{u}^{[0]}\in\mathbb{R}^{(NM)^2}$ and set $\boldsymbol{z}^{[0]}=\boldsymbol{T}\boldsymbol{u}^{[0]}$,
set $\tau>0$ and $\omega>0$ such that $\tau\left(\beta/2+\omega\lambda_g\|\boldsymbol{T}\|^2\right)<1$

For $l=0,1,\ldots$

$$\begin{cases} \widehat{\boldsymbol{u}}^{[l]} \;=\; \nabla f(\boldsymbol{u}^{[l]}) + \boldsymbol{T}^\top\boldsymbol{z}^{[l]} \\ \boldsymbol{u}^{[l+1]} \;=\; \boldsymbol{u}^{[l]} - \tau\,\widehat{\boldsymbol{u}}^{[l]} \\ \widehat{\boldsymbol{z}}^{[l]} \;=\; \boldsymbol{T}\big(2\boldsymbol{u}^{[l+1]} - \boldsymbol{u}^{[l]}\big) \\ \boldsymbol{z}^{[l+1]} \;=\; \big(\boldsymbol{z}^{[l]} + \omega\,\widehat{\boldsymbol{z}}^{[l]}\big) - \omega\,\text{prox}_{\frac{\lambda_g}{\omega}\|\cdot\|_{1,2}}\left(\dfrac{\boldsymbol{z}^{[l]}+\omega\,\widehat{\boldsymbol{z}}^{[l]}}{\omega}\right) \end{cases}$$

5. EXPERIMENTS

We test the proposed super-resolution algorithm with graph-based nonsmooth prior, *GB-NS* hereafter, on the *HCI light field dataset* [22], and we compare it to two state-of-the-art light field super-resolution algorithms: [10] and our previous algorithm *GB-SQ* [12]. The latter relies on a graph model of the light field as well, but binds it to a quadratic regularizer. We also provide the results of a simple bilinear interpolation of the single views as a baseline. Similarly to [10], we crop each light field to a 5×5 array of views, i.e., $M=5$.

The matrices $\boldsymbol{B}$ and $\boldsymbol{S}$ implement an $\alpha\times\alpha$ box filter and a regular sampler, respectively. For a fair comparison between

	Bilinear	[10]	GB-SQ	GB-NS
buddha	35.22	**39.12**	39.00	39.09
buddha2	30.97	33.63	34.41	**34.54**
couple	25.52	31.83	**33.51**	33.43
cube	26.06	30.99	**33.28**	33.11
horses	26.37	33.13	32.62	**33.59**
maria	32.84	37.03	**37.25**	37.02
medieval	30.07	33.34	33.45	**33.50**
mona	35.11	38.32	39.37	**40.05**
papillon	36.19	40.59	40.70	**41.56**
pyramide	26.49	33.35	**35.41**	35.09
statue	26.32	32.95	**35.61**	35.43
stillLife	25.28	28.84	**30.98**	30.96

Table 1. Mean PSNR on the HCI dataset [22], for $\alpha = 2$.

the methods GB-SQ and GB-NS, which rely on the same construction procedures for the warping matrices and the graph, we select the same parameter values: in Eq. (5) we set the size of the patch $\mathcal{P}$ to 7×7 pixels and $\sigma = 0.7229$. Finally, we empirically set $\lambda_2 = 0.15$ and $\lambda_g = 0.0055$ in the problem in Eq. (1) and solve it twice: at the first round, the warping matrices and the graph are built on a bilinearly interpolated version of the light field views, then, the obtained high resolution light field is used to build the warping matrices and the graph for the second round. Finally, for our experiments on the algorithm in [10] we use the code provided by the authors.

Due to space constraints, we report only the results of our experiment for the super-resolution factor $\alpha = 2$. For each light field in the HCI dataset, Table 1 reports the average PSNR [dB] of the M^2 reconstructed views. The proposed method GB-NS achieves the higher PSNR on five out of twelve light fields, and in the light fields `buddha` and `stillLife` it is no more than 0.03 dB away from the highest PSNR values, achieved by [10] and GB-SQ, respectively. Concerning the remaining five light fields `couple`, `cube`, `maria`, `pyramide` and `statue`, here the PSNR happens to be a misleading index, as in these light fields GB-NS achieves better visual results than its competitors [10] and GB-SQ. These five light fields share a particular structure: the foreground hosts an object that changes from light field to light field, while the background consists of the same panel with a fined detailed tree motif. At low resolution, the panel details are completely lost, and building a meaningful graph is really challenging, both for GB-NS and GB-SQ. In fact, no significant visual difference can be perceived between the panels reconstructed by GB-NS and GB-SQ. However, thanks to the smooth nature of its regularizer, GB-SQ reconstructs a smoother panel texture where the error is spread over the whole surface, and this biases the PSNR measure. On the other hand, in each one of the five considered light fields, the object in the foreground exhibits significantly sharper edges in the reconstruction by GB-NS than in those by GB-SQ and [10], where the same edges appear blurred and pixelated. An example is reported in Figure 5, which represents two details from the light fields `pyramide` and `statue`, where both the background and the foreground are visible.

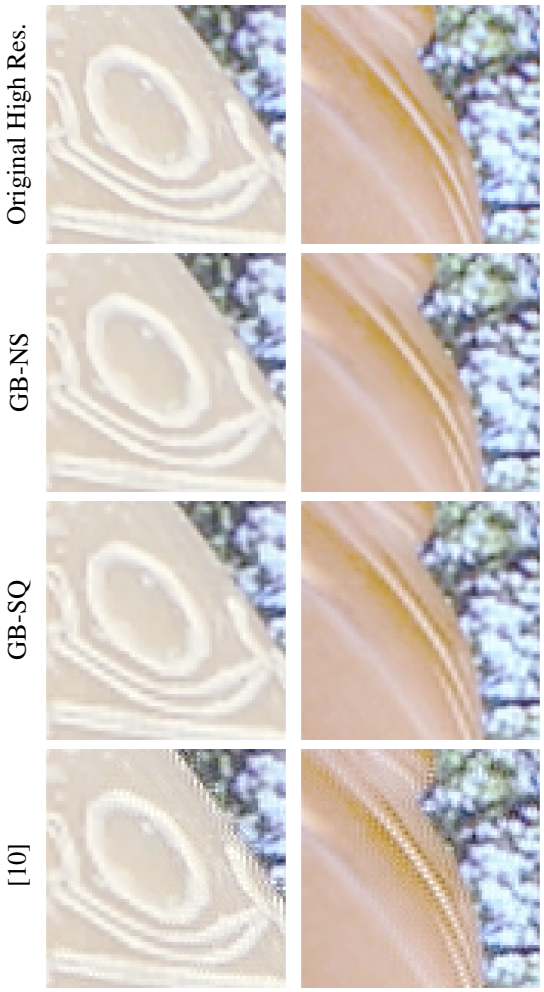

Fig. 2. Super-resolved details from the bottom right-most views of the light fields `pyramide` (left) and `statue` (right), for $\alpha = 2$. From the top to the bottom, the original High Resolution light fields and the reconstructions of GB-NS, GB-SQ and [10]. GB-NS provides sharper edges than its competitors GB-SQ and [10] in both the light fields.

6. CONCLUSIONS

We presented a new light field super-resolution algorithm that super-resolves all the light field views jointly, thanks to a graph-based regularizer that captures their correlation. In particular, we showed that coupling a graph model of the light field with a nonsmooth regularizer permits to reconstruct high resolution views characterized by a higher visual quality, often supported by the value of the PSNR. The proposed algorithm could further benefit from a non quadratic penalty in the warping term, as this could better handle the outlier pixels due the roughly estimated warping matrices.

7. REFERENCES

[1] R. Ng, M. Levoy, M. Brédif, G. Duval, M. Horowitz, and P. Hanrahan, "Light field photography with a hand-held plenoptic camera," *Computer Science Technical Report CSTR*, vol. 2, no. 11, pp. 1–11, Apr. 2005.

[2] M. Levoy and P. Hanrahan, "Light field rendering," in *Proceedings of the 23rd ACM annual conference on computer graphics and interactive techniques*, 1996, pp. 31–42.

[3] J. Yang, Z. Wang, Z. Lin, S. Cohen, and T. Huang, "Coupled dictionary training for image super-resolution," *IEEE Transactions on Image Processing*, vol. 21, no. 8, pp. 3467–3478, Aug. 2012.

[4] M. Bevilacqua, A. Roumy, C. Guillemot, and M. L. Alberi Morel, "Single-image super-resolution via linear mapping of interpolated self-examples," *IEEE Transactions on Image Processing*, vol. 23, no. 12, pp. 5334–5347, Dec. 2014.

[5] C. Dong, C. C. Loy, K. He, and X. Tang, "Image super-resolution using deep convolutional networks," *IEEE Transactions on Pattern Analysis and Machine Intelligence*, vol. 38, no. 2, pp. 295–307, Feb. 2016.

[6] M. Irani and S. Peleg, "Improving resolution by image registration," *CVGIP: Graph. Models Image Process.*, vol. 53, no. 3, pp. 231–239, Apr. 1991.

[7] S. Farsiu, M. D. Robinson, M. Elad, and P. Milanfar, "Fast and robust multiframe super resolution," *IEEE Transactions on Image Processing*, vol. 13, no. 10, pp. 1327–1344, Oct. 2004.

[8] T. Kohler, X. Huang, F. Schebesch, A. Aichert, A. Maier, and J. Hornegger, "Robust multiframe super-resolution employing iteratively re-weighted minimization," *IEEE Transactions on Computational Imaging*, vol. 2, no. 1, pp. 42–58, Mar. 2016.

[9] S. Wanner and B. Goldluecke, "Spatial and angular variational super-resolution of 4d light fields," in *European Conference on Computer Vision*. 2012, pp. 608–621, Springer.

[10] K. Mitra and A. Veeraraghavan, "Light field denoising, light field superresolution and stereo camera based refocussing using a GMM light field patch prior," in *Proceedings of the IEEE Conference on Computer Vision and Pattern Recognition Workshops*, 2012, pp. 22–28.

[11] M. Rossi and P. Frossard, "Graph-based light field super-resolution," in *IEEE 19th International Workshop on Multimedia Signal Processing*, 2017, pp. 1–6.

[12] M. Rossi and P. Frossard, "Light field super-resolution via graph-based regularization," *IEEE Transactions on Image Processing*, 2018, doi: 10.1109/TIP.2018.2828983.

[13] L. Condat, "A primal-dual splitting method for convex optimization involving lipschitzian, proximable and linear composite terms," *Journal of Optimization Theory and Applications*, vol. 158, no. 2, pp. 460–479, Aug. 2013.

[14] D. I. Shuman, S. K. Narang, P. Frossard, A. Ortega, and P. Vandergheynst, "The emerging field of signal processing on graphs: Extending high-dimensional data analysis to networks and other irregular domains," *IEEE Signal Processing Magazine*, vol. 30, no. 3, pp. 83–98, May 2013.

[15] A. Chambolle and T. Pock, "A first-order primal-dual algorithm for convex problems with applications to imaging," *Journal of Mathematical Imaging and Vision*, vol. 40, no. 1, pp. 120–145, May 2011.

[16] L. M. Briceño-Arias and P. L. Combettes, "A monotone+ skew splitting model for composite monotone inclusions in duality," *SIAM Journal on Optimization*, vol. 21, no. 4, pp. 1230–1250, Oct. 2011.

[17] P. L. Combettes and J. C. Pesquet, "Primal-dual splitting algorithm for solving inclusions with mixtures of composite, lipschitzian, and parallel-sum type monotone operators," *Set-Valued and Variational Analysis*, vol. 20, no. 2, pp. 307–330, Jun. 2012.

[18] B. C. Vũ, "A splitting algorithm for dual monotone inclusions involving cocoercive operators," *Advances in Computational Mathematics*, vol. 38, no. 3, pp. 667–681, Apr. 2013.

[19] N. Komodakis and J. C. Pesquet, "Playing with duality: An overview of recent primal-dual approaches for solving large-scale optimization problems," *IEEE Signal Processing Magazine*, vol. 32, no. 6, pp. 31–54, Nov. 2015.

[20] J. J. Moreau, "Fonctions convexes duales et points proximaux dans un espace hilbertien," *C. R. Acad. Sci.*, vol. 255, pp. 2897–2899, 1962.

[21] M. Hidane, M. El Gheche, J.-F. Aujol, Y. Berthoumieu, and C.-A. Deledalle, "Image Zoom Completion," *IEEE Transactions on Image Processing*, vol. 25, no. 8, pp. 3505–3517, Aug. 2016.

[22] S. Wanner, S. Meister, and B. Goldluecke, "Datasets and benchmarks for densely sampled 4d light fields," in *Proceedings of the VMV*, 2013, pp. 225–226.